Particle simulation of Alfvén waves excited at a boundary

F. S. Tsung, J. W. Tonge, and G. J. Morales
Physics and Astronomy Department, University of California, Los Angeles, Los Angeles, California 90095

(Received 30 July 2004; accepted 12 October 2004; published online 22 December 2004)

A particle-in-cell (PIC) code has been developed that is capable of describing the propagation of compressional and shear Alfvén waves excited from a boundary. The code is used to elucidate the properties of Alfvén wave cones radiated from sources having transverse scale comparable to the electron skin depth. Good agreement between theoretical predictions and simulation results is found over a wide range of frequencies. An investigation has been undertaken of the effect of hot ions on the Alfvén wave cones. The PIC simulations demonstrate that as the ion temperature is increased there is a reversal in the cone angle. The reversal implies that there is a cross-field focusing of the shear Alfvén waves. This is a feature which is presently being considered in studies of field-line resonances in the earth's magnetic field. The PIC results also illustrate the damping of shear modes due to the Doppler-shifted cyclotron resonance with hot ions. © *2005 American Institute of Physics*. [DOI: 10.1063/1.1832602]

I. INTRODUCTION

The interaction of Alfvén waves, both in the compressional and shear polarizations, with individual charged particles is presently a topic of significant interest in several areas of plasma science. The reason for the broad interest is that these waves provide a natural connection between macroscopic sources of free energy, such as currents and density gradients, and microscopic wave-particle processes (e.g., Landau damping and cyclotron resonance) that ultimately result in the generation of energetic particles and/or plasma heating. These interactions form the core of a variety of schemes for radio frequency heating[1] of magnetically confined plasmas and also for the generation of noninductive currents capable of sustaining the steady-state operation of tokamak devices. Of course, the interaction of energetic alpha particles with standing Alfvén waves is also a subject of concern[2] in assessing the operation of burning plasmas.

In contemporary studies of auroral dynamics the interaction of shear Alfvén waves of small transverse scale with ambient electrons is considered to play an important role.[3–5] A recent study[6] suggests that the acceleration of cold ionospheric ions by standing shear Alfvén waves can contribute significantly to the ion outflow away from the earth. Observations of the solar wind by spacecraft[7] consistently indicate that large amplitude Alfvén waves are a ubiquitous feature of these collisionless, flowing plasmas. Alfvénic wave-particle interactions are featured in studies of the solar corona[8] and they are being considered in the description of astrophysical processes.[9,10] Recently, an Alfvén wave maser has been realized in the laboratory[11] in which wave-particle interactions provide the amplification.

Although an extensive literature exists on the properties and consequences of Alfvén waves[12] in a wide variety of plasma environments for the most part the studies are based on magnetohydrodynamics (MHD) or fluid descriptions. Considerations of kinetic interactions associated with these waves have received relatively less attention and the investigations have primarily focused on linear features, sometimes complemented by test particle simulations.[13,14] Few investigations have considered the self-consistent simulation of the kinetic effects of ions and electrons and the associated nonlinearities. This is clearly a frontier and fertile area that is expected to receive increasing attention as the computational power improves.

The present study is the first step in a progressive development that aims to use particle-in-cell (PIC) computer simulations[15] to investigate, in a self-consistent manner, wave-particle interactions associated with Alfvén waves. The longer term goal, in anticipation of significant advances in computer hardware, is to develop a well-tested methodology that permits the study of frontier problems of relevance to laboratory and space environments in which large amplitude Alfvén waves are an important element.

This manuscript reports on the development of a PIC code useful in the investigation of Alfvénic interactions resulting from perturbations imposed at a boundary across the magnetic field. This is a situation that encompasses many features of interest to studies of the auroral ionosphere[16,17] as well as to basic laboratory experiments.[18,19] Quantitative tests are made on the excitation and propagation of compressional and shear modes in the linear regime where a good theoretical understanding exists. Special attention is devoted to the phenomenon known as "Alfvén wave cones."[20,21] The code is used to illustrate the effects produced by kinetic ions on these structures.

The manuscript is organized as follows. Section II describes the details and geometry of the computer code. Section III discusses the propagation of compressional modes while Sec. IV reports on the propagation of shear modes. The effects of kinetic ions is presented in Sec. V. Conclusions are given in Sec. VI.

II. SIMULATION MODEL

This investigation uses a particle-in-cell simulation model based on a code[22] (OSIRIS) previously developed to study laser-plasma interactions in unmagnetized plasmas.

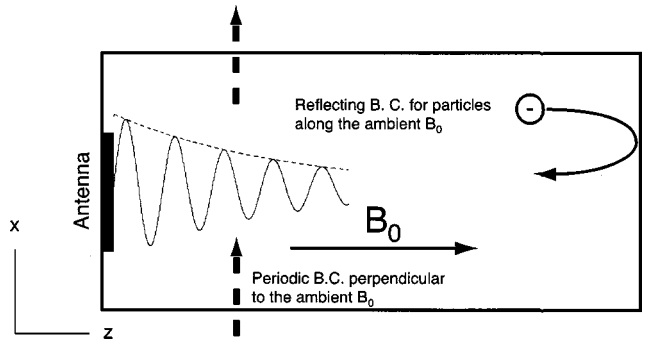

FIG. 1. Schematic of the geometry used in particle-in-cell code. System is periodic across the confinement magnetic field and finite in the parallel direction. Antenna prescribes a transverse spectrum at a specified frequency at the far left boundary and waves propagate toward the right boundary.

The code is written in an object-oriented style using FORTRAN90.[23] The present version of the code follows the self-consistent, relativistic motion of ions and electrons in the presence of a static confinement magnetic field that is spatially uniform. The code is fully electromagnetic and it allows the excitation of signals from antennas located at boundaries that intersect the confinement field. The results reported correspond to runs in 2-1/2 dimensions, i.e., the calculations follow two spatial coordinates and three velocity components for each particle. Limited, exploratory runs have also been performed in full three-dimensional (3-D) geometry. Typical cases reported here use $\approx 30\times 10^6$ (including ions and electrons) particles and are executed in the Blue Horizon supercomputer located in the San Diego Supercomputer Center. Meaningful results require runs of ≈600–800 CPU hours each. To expedite the analysis process, shorter complementary runs are performed for selected parameter choices in a local Mac cluster.

Figure 1 shows a schematic of the simulation geometry. The confinement magnetic field B_0 points along the z axis. In this direction the simulation box is finite while in the transverse x direction the system is periodic. The ignorable spatial direction corresponds to the y coordinate of the mutually orthogonal system (x,y,z) shown in the left corner of Fig. 1. On the far left side of the simulation box an antenna is located that is designed to launch Alfvén waves. When particles reach the boundaries along the z direction they are reflected with a new velocity vector chosen from a random number generator. The generator is adjusted to yield an effective temperature corresponding to the initial temperature of the plasma. This effectively decorrelates the particles from the incident fields and thus prevents the generation of runaway electrons due to boundary absorption. At the axial boundaries the transverse components of the fields are matched to vacuum using the finite scheme developed by Lindman.[24] For the low frequencies of relevance to Alfvén waves this procedure results in the reflection of the internally propagating signals.

The Alfvén wave antenna is modeled by prescribing the transverse electric field at the left boundary of the simulation box. By selecting the component of the prescribed field (x or y) it is possible to preferentially excite the shear mode (by selecting the x component) or the compressional mode (by selecting the y component). The functional form of the prescribed field component E_1 is

$$E_l(x,z=0,t)=E_0S(x/w)g(t/\tau)\cos(\omega t+\theta), \quad l=x,y, \quad (1)$$

where E_0 is the amplitude, ω is the wave frequency, and θ is the initial phase. The time-dependent function g provides a turn-on and turn-off capability with rise or fall-time τ which is typically chosen to be about one-half of the ion cyclotron period. The spatial shape factor S permits the excitation of various wave forms of interest having characteristic transverse scale w. For the studies reported here the typical choice is $S=\exp[-(x-x_0)^2/w^2]$ with x_0 defining the center of the pattern.

The electric field given by Eq. (1) is prescribed at a computational grid slightly offset towards the vacuum side from the actual terminating grid for the plasma particles. Its connection to the field inside the plasma is also accomplished through the Lindman scheme used at the right boundary. The combination of the Lindman scheme and the image current and polarization induced at the actual particle-boundary introduces a filtering of the Fourier spectrum in transforming from an applied electric field to a wave magnetic field. This implies that the self-consistent magnetic field that propagates in the plasma interior has a k_x spectrum that is modified from the prescribed E_1 spectrum. An example of this self-consistent distortion has been previously calculated for boundary excitations driven by a charged disk surrounded by a cold plasma.[20] For that case it is found that the imposed spectrum is multiplied by a Lorentzian whose width is the electron-skin depth. For the antenna excitation used in the PIC code a similar result is found, as is illustrated in Fig. 2.

The solid curve near the top of Fig. 2 corresponds to the prescribed electric-field spectrum used in the studies to be described later. The dotted curve is the spectrum of the magnetic field inside the plasma for a shear wave in the inertial regime having frequency $\omega=0.1\Omega_{ci}$. The dashed gray curve is the equivalent spectrum but at a higher frequency $\omega=0.5\Omega_{ci}$. The thinner curve towards the bottom shows the distortion that results on the previous curve when hot ions are present. The trend shown in Fig. 2 is consistent with a shielding of higher transverse wave numbers as the ion orbits become progressively more important. The consequence of the renormalized magnetic field spectra illustrated in Fig. 2 is that in comparing theoretical predictions to the results of the PIC simulation the appropriate "antenna spectrum" that must be used in evaluating the theory is the "renormalized magnetic spectrum" sampled at the actual particle boundary. That is the procedure followed in all the theoretical comparisons that appear later in the manuscript.

In selecting the parameter values for a particular study, a compromise must be found that permits the resolution of the spatial and temporal scales of relevance to Alfvénic phenomena while maintaining reasonable turn-around times in state-of-the-art computers. The results reported here are obtained with simulation boxes whose axial extent fit at least three to four parallel Alfvénic wavelengths and for time scales short compared to the development of axially standing waves. In

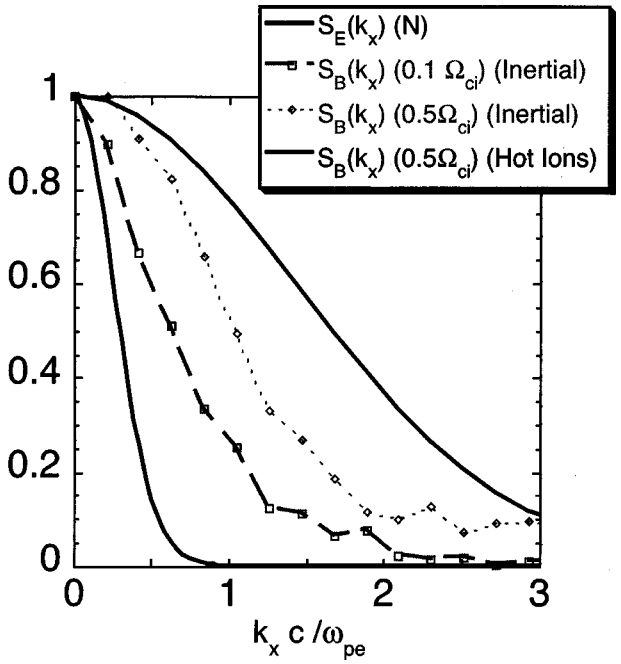

FIG. 2. Renormalized magnetic-field spectrum for shear waves. Top curve is transverse wave number spectrum of the prescribed electric field at the left boundary. Dotted curve below is the self-consistent spectrum of the wave magnetic field for $\omega=0.1\Omega_{ci}$ and dashed curve is for $\omega=0.5\Omega_{ci}$. The solid curve below the dash curve shows stronger filtering of large wave numbers caused by hot ions for $\omega=0.5\Omega_{ci}$.

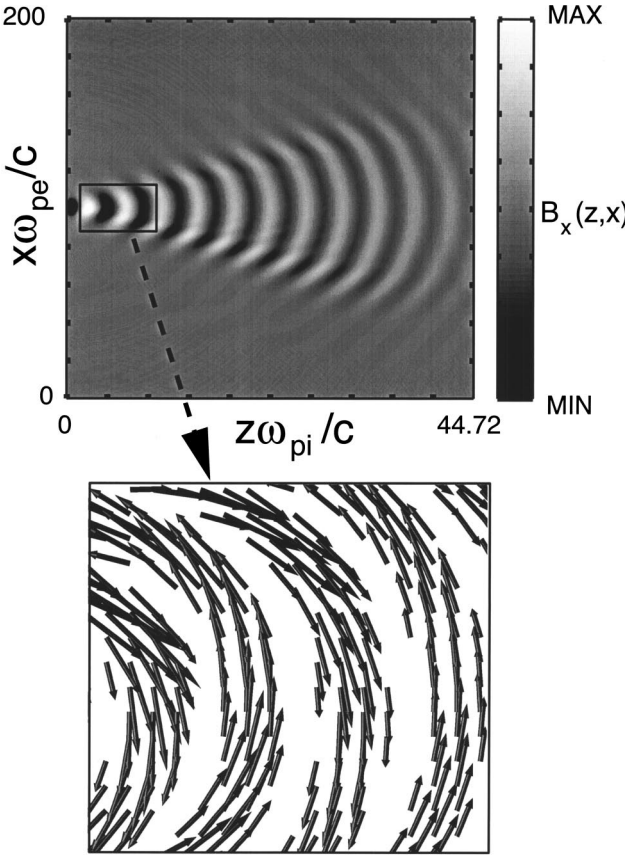

FIG. 3. Spatial pattern of excited compressional mode for $\omega=2.5\Omega_{ci}$ at a time $\omega t=57.5$. Top panel is contour of x component of wave magnetic-field (a.u.). Bottom panel displays wave magnetic-field vector within the small region indicated in top panel.

essence the studies approximate the propagation of Alfvén waves excited from a remote boundary into an infinitely long plasma. The dimension of the simulation box in the x direction is chosen carefully for each case studied in order to minimize the interference resulting from signals excited in the neighboring periodic cell. For instance, in the investigation of compressional modes the transverse box size is typically 200 electron-skin depths (c/ω_{pe}), while in the study of inertial Alfvén cones the size is $30c/\omega_{pe}$. In all the simulation results reported here the spatial grid size is $0.1c/\omega_{pe}$ and the time step is $0.06c/\omega_{pe}^{-1}$, where c is the speed of light and ω_{pe} is the electron plasma frequency.

The degree of magnetization of the plasma is represented by the ratio of the electron cyclotron frequency to the electron plasma frequency Ω_{ce}/ω_{pe} which for all the cases reported has a value of 0.4. This value is characteristic of a wide variety of systems of physical interest. At present the computational power available limits the studies to an ion to electron mass ratio $M/m=20$. This is a practical compromise that allows a reasonable separation of the time scales of interest, namely, $\omega_{pe}>\Omega_{ce}>\omega_{pi}\gg\Omega_{ci}$, where ω_{pi} is the ion plasma frequency and Ω_{ci} is the ion cyclotron frequency. It is anticipated that within a few years significant advances in computational power will permit the exploration of more realistic mass ratios while following the detailed electron dynamics. With these parameter choices the ratio of the Alfvén speed to the speed of light is $v_A/c=0.097$. Since all the cases reported correspond to cold electrons this implies that the Alfvén modes sampled are in the inertial electron regime. To facilitate the comparison of the numerical studies, the spatial scales in all the figures are scaled to universal quantities. The axial z dependence is scaled to the ion skin-depth c/ω_{pi} and the transverse x dependence to c/ω_{pe}. This implies that in all the figures shown there is a built-in contraction of the parallel dependencies, as is appropriate for the modes investigated.

III. COMPRESSIONAL MODE

This section explores the propagation of compressional Alfvén waves excited from a boundary at a frequency above the ion cyclotron frequency, i.e., in a frequency interval in which the shear mode does not propagate. A distinguishing feature of the compressional mode is that it propagates from a source in a nearly isotropic pattern with its electric field exhibiting circular polarization in the right-hand sense relative to the confinement magnetic field. To accommodate the characteristic isotropic spreading of this mode the PIC simulation is run with a relatively large computational box. For the chosen antenna frequency of $\omega=2.5\Omega_{ci}$ the axial length of the box used is ten wavelengths and the transverse box dimension is $200c/\omega_{pe}$. The antenna is excited in the E_y polarization with a transverse scale $w=1.0c/\omega_{pe}$. The ions and electrons are cold, i.e., $\rho_i=\rho_e=0$, where ρ_j is the Larmor radius for species j.

Figure 3 displays the two-dimensional spatial pattern of the wave magnetic field in the x direction, i.e., $B_x(x,z)$ at a fixed time $\omega t=57.5$, as obtained from the PIC simulation for

the previously described excitation scheme. The top panel clearly illustrates that the self-consistent response of the plasma to the boundary modulation results in a propagating mode with nearly isotropic spreading. The bottom panel in Fig. 3 provides an expanded view of the wave magnetic-field vector within the small region indicated. It demonstrates that at a fixed time the wave field oscillates in space and that it has two components x and z within the plane of propagation. This result implies that the self-consistent plasma response is of the compressional type since it gives rise to a modulation in the strength of the confinement magnetic field. This behavior is to be contrasted to the shear polarization, discussed later in Sec. IV, in which the fluctuating magnetic field is perpendicular to the plane of propagation. It is to be noted further that a normalized antenna field of strength $cE_y(z=0, x=x_0)/(B_0 v_A)=0.1$ results in compressional disturbances having time asymptotic, fractional fluctuations in the magnetic field of magnitude $|\delta B|/B_0=0.05$.

The polarization of the wave electric field corresponding to the spatial pattern of Fig. 3 is shown in Fig. 4(a). This presentation consists of a spatial hodogram of the transverse electric field components E_y and E_x at a fixed x position ($x=100c/\omega_{pe}$) across the confinement magnetic field. The axial position z is the variable parameter, analogous to the time in an oscilloscope display. It should be noted, however, that in a spatial hodogram the sense of rotation is reversed from that expected for a temporal hodogram. The reason is that for a wave propagating in the positive z direction with wave number k_z the phase factor $\theta=\omega t-k_z z$ decreases as z increases for a fixed time t. Thus the right hand, temporal rotation predicted by linear theory for a compressional mode should appear in a spatial hodogram as a left-hand rotation. In Fig. 4(a) it is seen that the spatial hodogram corresponds to a spiral pattern that winds in the clockwise direction relative to the z direction (out of the page). The points associated with larger amplitudes are close to the antenna while the points with smaller amplitude are far from the antenna. The clockwise sense of rotation indeed corresponds to the predicted right-hand, temporal polarization for this mode. The decrease in field amplitude with axial position leading to the decrease in the radius of the spiral pattern in Fig. 4(a) is predominantly determined by the geometrical spreading of the wave.

Figure 4(b) compares the total wave-current density (dark diamonds) in the y direction to the contribution from the $\mathbf{E}\times\mathbf{B}_0$ drift of the electrons (solid line) at positions along the spatial hodogram shown in Fig. 4(a). It is this component of the current that is responsible for the generation of the wave magnetic field vector displayed in the bottom panel of Fig. 3. The current density is scaled to $en_0 v_A$ where e is the quantum of charge, n_0 is the plasma density, and v_A is the Alfvén velocity. Hence it represents the effective velocity in the y direction. It is seen that the self-consistent result from the PIC simulation indicates that the electron drift primarily determines the wave current, as is expected, since the ion response at this frequency is practically unmagnetized.

Figure 5(a) provides a comparison of the theoretical dispersion relation for a compressional mode to the results of the PIC simulation. The dashed line displays the dependence of the scaled parallel wave number $k_x c/\omega_{pi}$ on the scaled

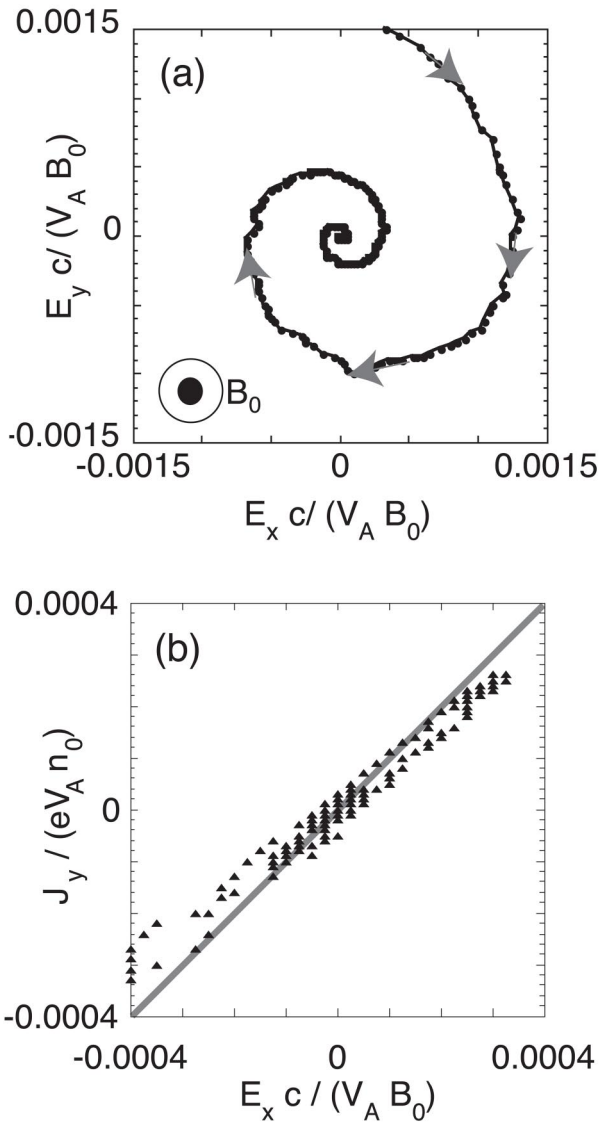

FIG. 4. (a) Spatial hodogram of y and x components of scaled wave electric field associated with the compressional mode pattern shown in the top panel of Fig. 3 indicates that the mode is right-hand polarized (explained in text). The parameter along the spiral curve is the axial position z; large field values are near the antenna and small values are in the asymptotic propagation region. Decrease in amplitude results from approximate isotropic spreading. The hodogram is projected at a fixed transverse position $x\omega_{pe}/c=100$. (b) Dependence of y component of the scaled plasma current density on scaled value of x component of wave electric field. Diamonds are simulation results and solid line is theoretical prediction. The values are obtained along the points of the spatial hodogram in part (a).

transverse wave number $k_x c/\omega_{pe}$. This is the exact analytic solution to the quartic equation obtained from the general dispersion relation for a cold magnetized plasma,

$$k_z^+ = \frac{\omega}{c}\sqrt{\varepsilon_\perp + \frac{-b+(b^2+4ad)^{1/2}}{2a}}, \tag{2}$$

where the coefficients are $a=\varepsilon_\parallel/(\varepsilon_\parallel-k_x^2c^2/\omega^2)$, $b=k_x c/\omega[(-\varepsilon_\parallel-\varepsilon_\perp)/(k_x c/\omega-\varepsilon_\parallel)]$, and $d=[\varepsilon_\parallel-(k_x^2c^2/\omega^2\varepsilon_\perp)/(k_x c/\omega-\varepsilon_\parallel)]$, with the ε_j the well-known components of the cold, magnetized dielectric tensor.[25] The diffuse gray-colored blotches in Fig. 5(a) correspond to the two-dimensional Fourier spectrum of the spatial wave pat-

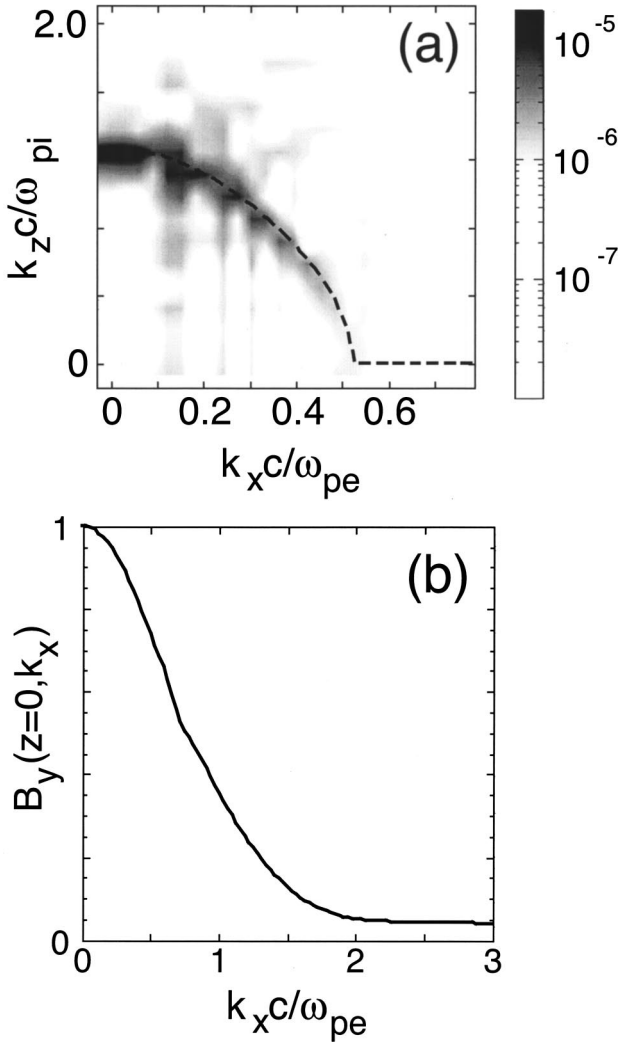

FIG. 5. (a) Dashed curve is the theoretical dispersion relation of compressional mode for parameters leading to the wave pattern of Fig. 3. The flat portion at larger k_x indicates evanescent region. Gray-scale blotches correspond to the Fourier spectrum of the wave pattern shown in the top panel of Fig. 3. It demonstrates that the excited wave spectrum propagates along the theoretically predicted characteristics. (b) Spectrum of B_y measured at the boundary of the simulation $B_y(z=0,k_x)$. Note the larger k_x scale displayed in comparing to part (a).

tern shown in Fig. 5(a). The wave spectrum is shown in the logarithmic gray scale indicated on the right side of Fig. 5(a). It is seen that the power spectrum obtained in the PIC simulation follows closely the theoretical dispersion relation.

Another significant feature seen in Fig. 5(a) is that no Fourier components are found to be present in the radiated wave pattern beyond the theoretically predicted cutoff for the mode at $k_x=0.559\omega_{pe}/c$. This occurs in spite of the antenna spectrum, shown in Fig. 5(b), having sizeable power available in wave numbers larger than this cutoff value. It should also be mentioned that for these parameters, there is a finite contribution from the off-diagonal element of the dielectric tensor due to the fact that the electrons are magnetized while the ions are not. The exact dispersion deviates from the ideal MHD approximation $k_A^2=k_\parallel^2+k_\perp^2$, which is isotropic in (k_x,k_x) space. This can be inferred from a closer examination of the radiation pattern in Fig. 3.

IV. SHEAR MODE

This section extends the scope of Sec. III to frequencies below the ion cyclotron frequency, i.e., $\omega<\Omega_{ci}$. In this regime the compressional mode exhibits a cutoff at a relatively small transverse wave number, thus for an antenna whose transverse dimension is on the order of the electron skin depth (as is the case in this study) the dominant mode excited has shear polarization. Of course, there is always a small parasitic excitation of a $k_x=0$ component that appears as a propagating compressional mode, as is shown later.

A significant property of shear modes is the weak dependence of k_z on k_x, leading to a nearly field-aligned propagation, and no perturbed parallel magnetic field. Thus, to accommodate the filamentary nature of these waves in a computer simulation, especially at low frequencies, it is necessary to use simulation boxes whose axial extent is much larger than the transverse dimension. Also, in displaying the results a different scaling must be used for the z and x coordinates.

Next, two representative cases of shear mode propagation in a cold plasma (inertial regime) are presented. The plasma parameters used here are identical to those from the preceding section, but the dimensions of the simulation box are changed to accommodate the field-aligned propagation of the shear mode. One corresponds to a relatively low frequency $\omega=0.1\Omega_{ci}$ while the other is in a regime where off-diagonal contributions from the dielectric tensor begin to be significant, i.e., $\omega=0.5\Omega_{ci}$. The antenna is energized through the E_x component with a transverse scale $w=1.0c/\omega_{pe}$. The peak electric field at the left boundary is $0.15B_0v_A/c$ for both cases. This results in asymptotically propagating magnetic fields whose fractional amplitude $|\delta B_y|/B_0$ are in the range of 0.03 (for the $0.5\Omega_{ci}$ case) and 0.08 (for the $0.1\Omega_{ci}$ case). The size of the simulation box is $[1.56.5c/\omega_{pi}, 30c/\omega_{pe}]$ for the $0.1\Omega_{ci}$ case and $[31.31c/\omega_{pi}, 30c/\omega_{pe}]$ for the $0.5\Omega_{ci}$ case. Both systems accommodate approximately three wavelengths along the confinement magnetic field.

Figure 6 displays the two-dimensional spatial pattern of the shear modes excited. The top panel is the $0.1\Omega_{ci}$ case and the bottom panel is the $0.5\Omega_{ci}$ case. The quantity displayed in a linear gray-scale contour is $B_y(z,x)$ at a fixed time $\omega t=23.4$ (for the $\Omega_{ci}=0.5$ case) and $\omega t=23.6$ (for the $\Omega_{ci}=0.1$ case), which is slightly smaller than one transit time through the respective boxes. The darker shades correspond to positive values and the lighter ones to negative values. The dashed white lines in Fig. 6 are the Alfvén cone characteristics that are theoretically predicted[20] to describe the spreading of shear Alfvén waves excited at a boundary in a cold plasma (inertial regime). The cone angle θ_c is given by $\tan(\theta_c)=(\Delta x/Lz)=\omega/\Omega_{ci}\sqrt{m_e/\{M_i[1-(\omega_0/\Omega_{ci})^2]\}}$ (where Δx is the transverse spread of the shear wave over an axial distance L_x). It is seen that the PIC results agree with the theoretical prediction over a considerable range of frequency variation (factor of 5) and thus complement the laboratory measurements[18,19] of this effect.

A more detailed comparison between the PIC simulation (black triangles) and the theory of Alfvén wave propagation

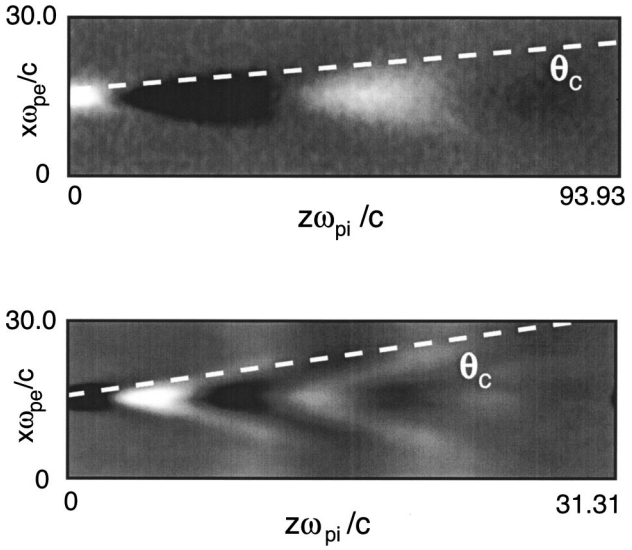

FIG. 6. Inertial cone patterns generated for shear modes excited at two different frequencies $\omega=0.1\Omega_{ci}$ (top panel) and $\omega=0.5\Omega_{ci}$ (bottom panel). Quantity displayed in linear gray-scale contours is y component of wave magnetic field at a fixed time. Dashed line is the theoretically predicted cone angle. Note the different ranges in the axial direction used in the two panels, as is necessary to accommodate the different cross-field spreading rates.

(dashed curve) is shown in Fig. 7. This displays corresponds to the axial variation of the perturbed magnetic field $B_y(z,x)$ shown in the top panel of Fig. 6 at a fixed transverse position $x=15c/\omega_{pe}$. The theoretical result corresponds to the asymptotic signal calculated from the boundary perturbation $S(x)\equiv B_y(z=0,x)$ in a manner analogous to the technique previously developed[20] to describe laboratory results. The difference here is that the periodicity of the simulation in the x direction needs to be considered. The appropriate expression for a periodic system with a finite number of grid points is

$$B_y(z,x)=\mathrm{Re}\left[\frac{1}{Nx}\sum_{k_x}\exp\{i[k_x^-(k_x)z+k_xx]\}\sum_x S(x)\times\exp[-ik_xx]\right], \tag{3}$$

where the summation over x indicates summing over all the simulation grids in the $\hat{x}$ direction (from 1 to Nx), and the sum over k_x sums over all modes in the first Brillouin zone. The parallel wave number $k_z^-(k_x)$ now corresponds to the negative branch of one of the quadratic roots of the general dispersion relation, i.e.,

$$k_z^-=\frac{\omega}{c}\sqrt{\epsilon_\perp+\frac{-b-(b^2+4ad)^{1/2}}{2a}}, \tag{4}$$

where a, b, and d have been previously defined in Eq. (2). It is seen from Fig. 7 that the theoretical prediction is in good agreement with the PIC result in the asymptotic region far from the antenna but deviations arise near the antenna.

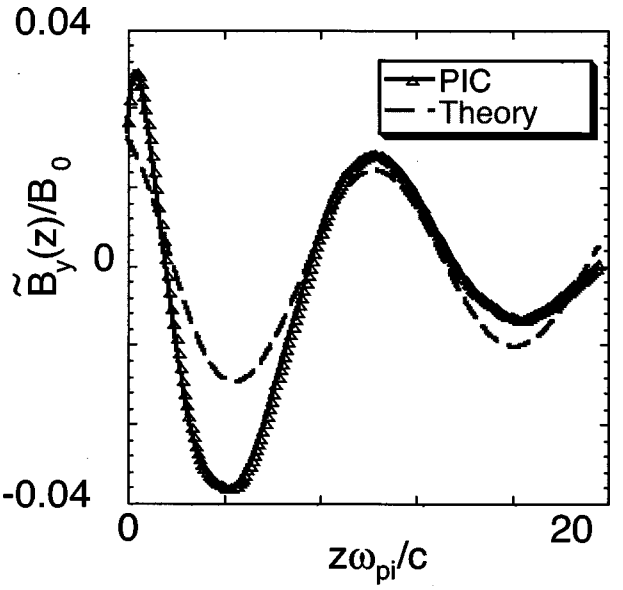

FIG. 7. Axial dependence of cone pattern for the case displayed in the top panel of Fig. 6 along a fixed transverse position $x=15c/\omega_{pe}$. Dashed line is theoretical prediction explained in text and dark connected diamonds are simulation results.

The self-consistent particle responses are illustrated in Figs. 8(a)–8(c). Figure 8(a) shows the spatial pattern of the perturbed magnetic field $B_y(z,x)$ over one axial wavelength (for the $\omega=0.5\Omega_{ci}$ case). To satisfy Ampère's law a right-handed current loop must accompany each structure seen in Fig. 8(a), as is illustrated in Figs. 8(b) and 8(c). The dark curve in Fig. 8(b) displays the transverse dependence of $B_y(z=3.2c/\omega_{pi},x)$ (in arbitrary units) along the dark dashes in Fig. 8(a). The dashed curve in Fig. 8(b) is the scaled, average z component of the electron velocity $\langle v_z(z=3.2c/\omega_{pi},x)\rangle_a/c$ along the same cut. This quantity clearly shows the formation of counter-propagating, parallel electron current filaments which surround the perturbed magnetic field. The polarization drift of the ions must close this current loop near the location where $B_y(z,x)$ changes sign (i.e., where it crosses the value 0). This behavior is demonstrated in Fig. 8(c) using a spatial hodogram [along the white dashes of Fig. 8(a)] of $B_y(z,x=15c/\omega_{pc})$ and the averaged, x component of the ion velocity $\langle v_x(z,x=15c/\omega_{pc})\rangle_i$. Figure 8(c) shows that the x component of the ion velocity is largest in regions where the perturbed magnetic field vanishes, and that no ion flow occurs in regions where the perturbed magnetic field is largest. The sense of rotation of the hodogram describing the ion motion can be obtained from the linearized Ampère's law, i.e., $-ik_xB_y\sim en_0\langle v_x\rangle_i$ from which it can be deduced that the simulation results agree with theoretical predictions.

In Figs. 9(a) and 9(b) comparisons are made between the two-dimensional Fourier spectrum of the radiated signal and the dispersion relations for the shear and compressional branches, k_z^- and k_z^+, respectively. The comparisons are made for the $\omega=0.5\Omega_{ci}$ case at a time $\omega t=23.4$. By this time the wave has filled the simulation box, therefore the transforms can be interpreted as the spatial Fourier spectrum of the time-asymptotic radiation pattern. The propagating roots, i.e., the real parts of the solutions traveling away from the antenna are shown as continuous curves, i.e., $\mathrm{Re}(k_z^+)$ (in black) and

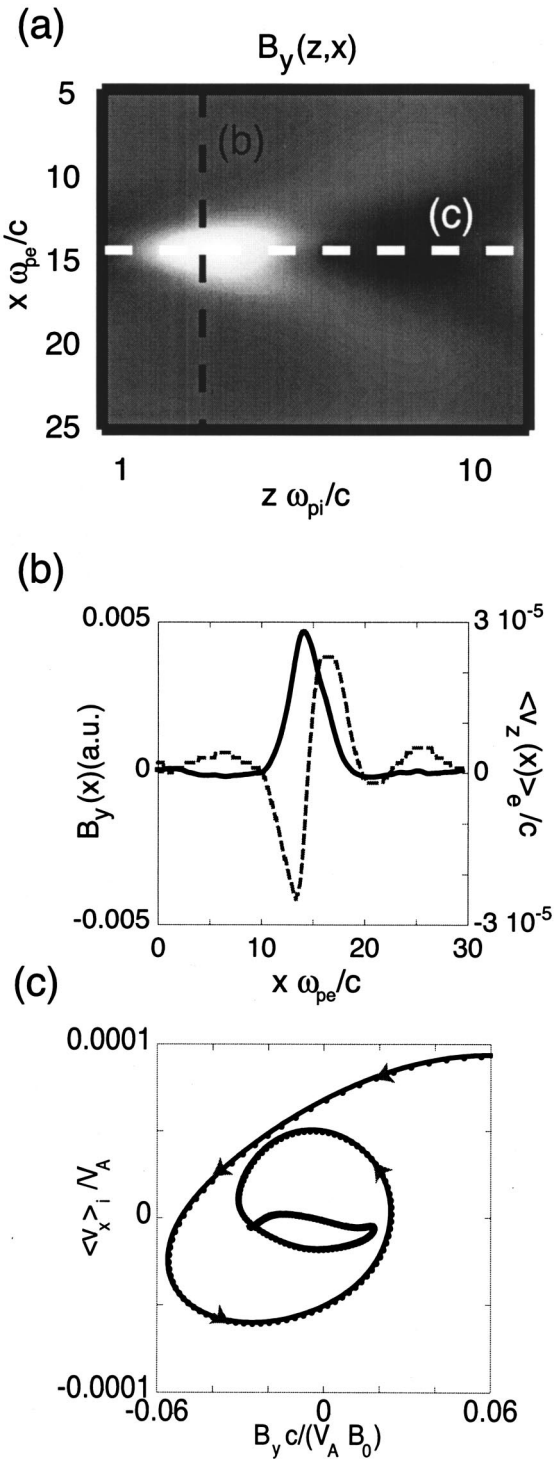

FIG. 8. Illustration of self-consistent particle currents for shear mode. (a) Spatial pattern of wave magnetic field over one wavelength for the $\omega = 0.5\Omega_{ci}$ case. (b) Dark solid curve shows transverse variation of wave magnetic field along the dark dashes in (a). Dashed curve is scaled, average electron velocity along the parallel direction projected also along the dark dashes. It demonstrates the formation of thin current filaments of opposite polarity along the confinement magnetic field. (c) Spatial hodogram of average ion current in x direction and wave magnetic field along the white dashes in (a). It shows transverse ion current is out of phase with magnetic field in such a manner as to close the current loop connected to the axial electron current filaments.

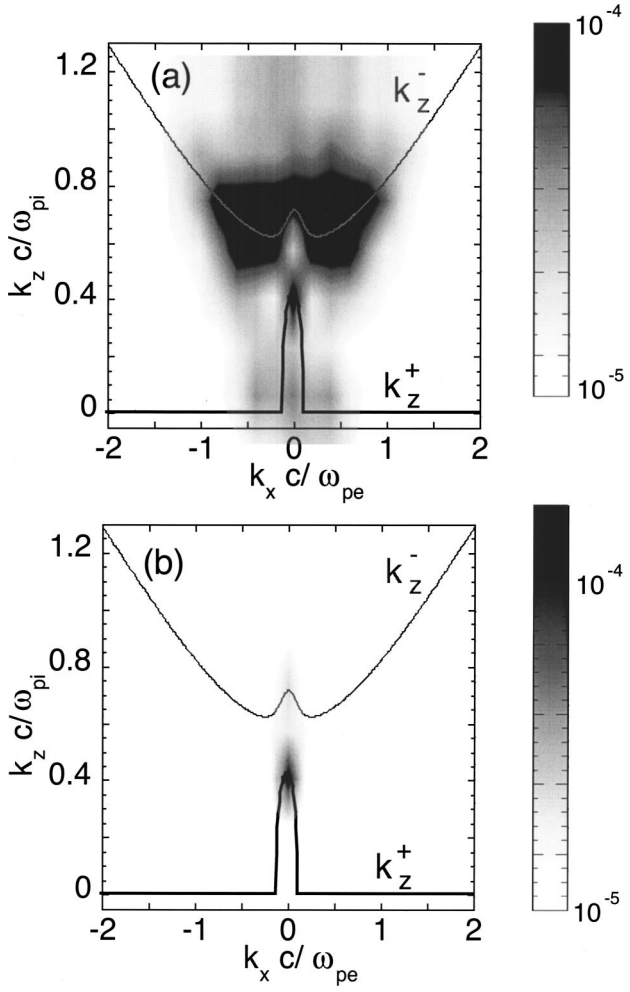

FIG. 9. Simultaneous excitation of shear and compressional modes from a prescribed x component electric field at $\omega = 0.5\Omega_{ci}$ having a broad k_x spectrum at the antenna. (a) Smeared blotches on linear gray-scale correspond to the two-dimensional Fourier spectrum of the y component of the wave magnetic field under steady-state conditions in which the pattern fills the entire computational box. Continuous curves correspond to the theoretical dispersion relations for the shear mode (top curve) and compressional mode (bottom curve). (b) Similar presentation for the x component of the wave magnetic field. Result demonstrates that antenna in this mode of excitation predominantly excites a shear mode but there is a parasitic radiation of a compressional mode near $k_x = 0$.

$\mathrm{Re}(k_z^-)$ (in gray). The smeared black-gray blotches correspond to the spatial Fourier spectrum of the instantaneous magnetic field components. Figure 9(a) compares the transform of the y component $B_y(k_z, k_x)$, and Fig. 9(b) compares the transform of the x component $B_x(k_z, k_x)$. It is to be emphasized that in the case examined the antenna excitation occurs through the application of an oscillating electric field in the x direction and the plasma is free to respond to it. There is no *a priori* restriction as to what branch of propagation should be excited. The plasma, through its dispersive properties, determines the mix of modes that are radiated in the steady state.

It is seen from Fig. 9(a) that signals with significant B_y are radiated all along the shear-mode dispersion relation and follow in detail the theoretically-predicted curvature of this mode in the small k_x region. It is also seen that a compressional mode with a B_y component is simultaneously radiated by the antenna, but it has essentially $k_x=0$. The significance of this result is that for frequencies below the ion cyclotron frequency, boundary excitation through E_x has an intrinsic mixture of short transverse scales embedded in a larger scale. This mixing can have consequences for large amplitude excitation and associated nonlinear evolution.

Figure 9(b) complements the perspective obtained from Fig. 9(a). It shows that the significant B_x radiated is carried away along the compressional branch. There is only a faint trace that a small parasitic excitation along the shear branch occurs, but it is confined to the complementary $k_x=0$ region. This is consistent with the fact that the shear mode does not have a magnetic field component along the confinement magnetic field.

V. HOT ION EFFECTS

This section considers the effects of hot ions on the properties of shear Alfvén waves excited by a localized source. This is a topic of contemporary interest in studies of auroral dynamics and is generic to the behavior of high-β plasmas. In the context of the present study the ions are considered to be "hot" when the ion Larmor radius $\rho_i = v_{ti}/\Omega_{ci}$ is comparable or larger than the electron skin depth, i.e., $\omega_{pe}\rho_i/c \geqslant 1$, where v_{ti} is the ion thermal velocity. In this regime the direction of the cold-cone pattern illustrated in Sec. II is reversed. Instead of the cones causing the transverse spread of wave energy, in the kinetic ion regime the cones result in the focusing of wave energy across the confinement magnetic field. This effect has been recently proposed[26] as a mechanism that provides latitudinal localization for field-line resonances excited in the earth's magnetic field. In addition, for high-β plasmas in which the ion thermal velocity is a significant fraction of the Alfvén speed, the process of ion cyclotron resonance can have an important effect on waves whose frequency is comparable to the ion cyclotron frequency. The plasma parameters for the simulations presented in this section are nearly identical to those in the preceding section, except that the ions are hot and have a thermal velocity of $0.24v_A$, which corresponds to an ion beta of $\beta_i = 8\pi n_0 M_i v_{ti}^2/B_0^2 = 2(v_{ti}/V_A)^2 = 0.115$. The ion Larmor radius is $1.1c/\omega_p$.

The effect of kinetic ions on the dependence of the parallel wave number k_z of a shear Alfvén wave on the wave number across the confinement field k_x is illustrated in Fig. 10 for a wave frequency $\omega=0.5\Omega_{ci}$ and a representative ion to electron mass ratio of 2000. This choice of a mass ratio is

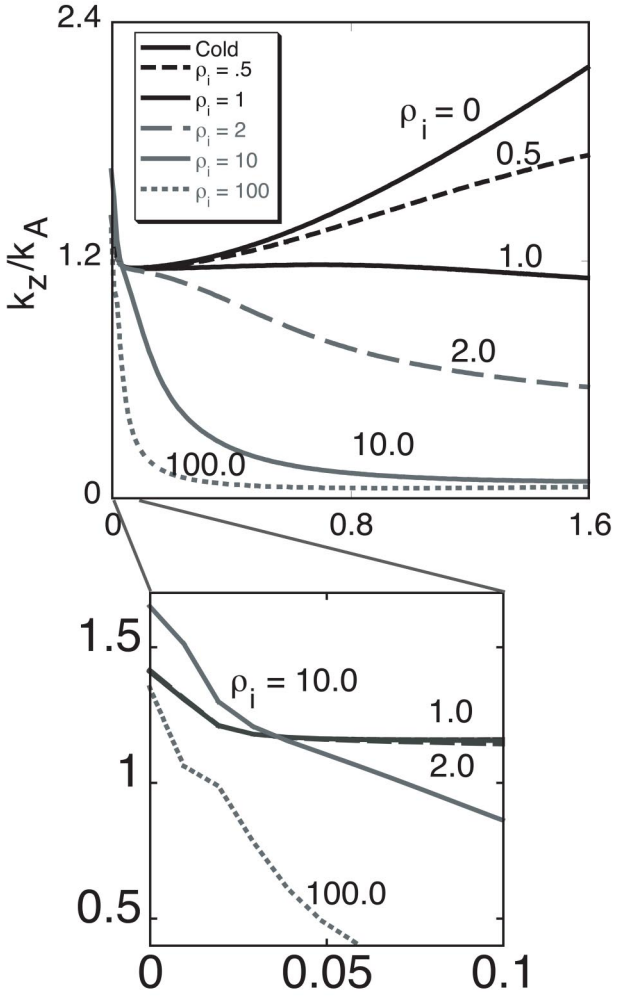

FIG. 10. Effect of hot ions on the shear mode dispersion relation for a nominal mass ratio $M/m=2000$ and $\omega=0.5\Omega_{ci}$. Top curve corresponds to cold ions and bottom one to extremely hot. Larmor radius indicated is scaled to c/ω_{pe}. Transition from positive to negative slope of curves indicates a reversal in the inertial cone angle resulting in transverse focusing. Inset shows topology in the small transverse wave number regime explained in text.

meant to convey the universal features that are expected in a realistic plasma environment. The specific case for simulation conditions is shown in Fig. 11. Both of these figures are generated using the dispersion relation

$$(n_z n_x)^2(n^2-\epsilon_{xx}) - (n_x^2-\epsilon_{xx})[(n_z^2-\epsilon_{xx})(n^2-\epsilon_{xx}) + \epsilon_{xy}^2] = 0, \tag{5}$$

where the index of refraction n is given by $\sqrt{n_x^2+n_z^2}$ with $n_z = ck_z/\omega$, $n_x = ck_x/\omega$, and $k_y \equiv 0$. The z direction is parallel to the confinement magnetic field, and the x and y directions are transverse, as indicated in Fig. 1. The components of the dielectric tensor for a plasma consisting of cold electrons and hot (Maxwellian) ions are given by[27]

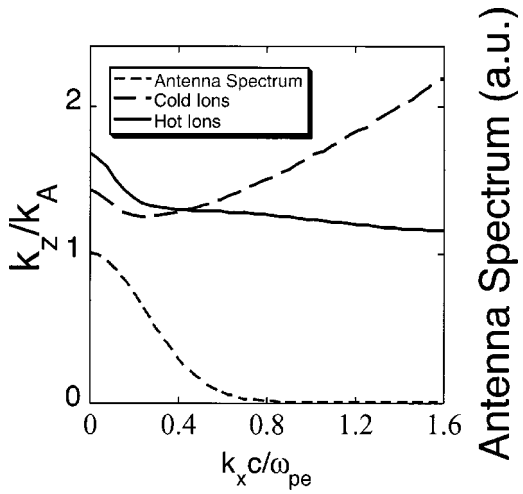

FIG. 11. Top two curves show theoretical dependence of scaled axial wave number on scaled transverse wave number for cold ions (dashed) and for a hot ion population (solid) with $\rho_i\omega_{pe}/c=1.1$. The reversal in slope of these two curves imply a change in the topology of the propagation cones, as is illustrated in Fig. 13. The dashed curve at the bottom is the effective antenna spectrum for the simulation used in the calculation presented in the bottom panel of Fig. 13. Parameters correspond to simulation choices in Sec. II, $\omega=0.5\Omega_{ci}$.

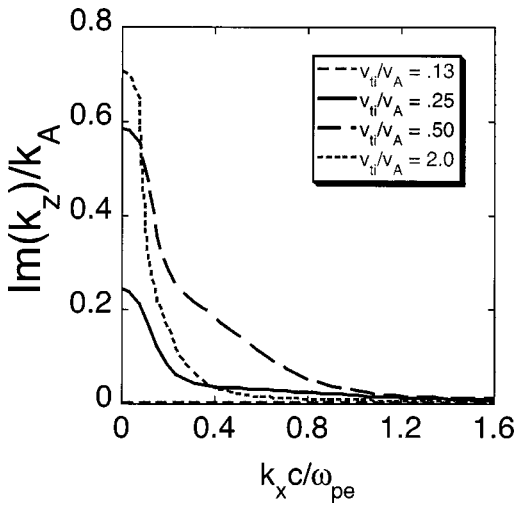

FIG. 12. Theoretical prediction of the dependence of scaled axial-damping decrement on scaled transverse wave number for different ion temperatures. Parameters correspond to simulation choices in Sec. II, $\omega=0.5\Omega_{ci}$. This damping is an effect of cyclotron resonance; it depends on ion beta for fixed finite ω/Ω_{ci}.

$$\epsilon_{zz} = 1 - \omega_{pe}^2/\omega^2,$$

$$\epsilon_{xx} = \epsilon_{yy} = 1 + \frac{\omega_{pi}^2}{\omega\sqrt{2}k_x v_{ti}} \frac{e^{-\lambda_i^2}}{\lambda_i^2} \sum_m m^2 I_m(\lambda_i^2) Z(\xi_{im}),$$

$$\epsilon_{xy} = -\epsilon_{yx} = i\left\{ \frac{\omega_{pe}^2 \Omega_{ce}}{\omega(\omega^2 - \Omega_{ce}^2)} - \frac{\omega_{pi}^2}{\omega\sqrt{2}k_z v_{ti}} \frac{e^{-\lambda_i^2}}{\lambda_i^2} \sum_m m[I_m(\lambda_1^2) - I_m'(\lambda_i^2)] e^{-\lambda_i^2} Z(\xi_{im}) \right\}, \quad (6)$$

where $\lambda_i = k_x v_{ti}/\Omega_{ci}$, $\xi_{im} = (\omega - m\Omega_{ci})/\sqrt{2}k_x v_{ti}$, Z is the plasma dispersion function, I_m is the modified Bessel function of order m, and I_m' is its first derivative with respect to the argument.

The top panel of Fig. 10 displays a sequence of dispersion curves in which the ion temperature (i.e., ρ_i scaled to the electron skin depth) is increased. The top curve corresponds to cold ions and the bottom to extremely hot ions. It is seen that for the cold-ion case k_z exhibits an asymptotic linear increase with k_x. This is the classic regime of inertial Alfvén cones studied in Sec. IV. As the ion temperature is increased the slope of the asymptote decreases, close to the critical value of $\rho_i = c/\omega_{pe}$ (solid curve) the slope reverses sign. Physically this slope reversal means that the sense of the spreading cones in configuration space is reversed from that obtained in the inertial case. As the ion temperature is increased beyond the critical value the slope of the inverted kinetic cones also increases.

The bottom panel of Fig. 10 provides an enlarged view of the behavior in the small transverse wave number region to illustrate that kinetic effects are also present in this limit. The origin of this dependence can be traced to the finite frequency of the signal considered and is physically related to the removal of the cancellation of the ion and electron $\mathbf{E}\times\mathbf{B}$ currents, which is enhanced by the finite ion Larmor radius corrections to ϵ_{xy}.

The top two curves in Fig. 11 represent the dependencies illustrated in Fig. 10 for the specific parameter choices used in the PIC simulation. The wave frequency has the same value as in Fig. 10 ($\omega=0.5\Omega_{ci}$) but the significant difference is the lower ion to electron mass ratio of 20 (a factor of 10 smaller). The consequence of the smaller mass ratio is that the features seen in the bottom panel of Fig. 10 extend over a larger range of perpendicular wave numbers. The cold-ion curve (top dashed curve) shows the asymptotic inertial cone behavior while the solid curve ($\rho_i = 1.1c/\omega_{pe}$) clearly shows the reversal in slope associated with hot ions. The bottom curve in Fig. 11 corresponds to the renormalized antenna spectrum (described in Sec. II and illustrated in Fig. 2) used in the PIC simulation. It is concluded from the overlap of the top curves with a significant fraction of the spectrum that the theoretically predicted reversal of the Alfvén cones is amenable to investigation with a PIC simulation that uses the lower mass ratio.

For the case of finite frequency and hot ions sampled in the PIC simulation the cyclotron resonance causes spatial damping of the wave which is quantified by an imaginary part of k_z. Figure 12 shows the dependence of the theoretically predicted imaginary part on the perpendicular wave number for different values of v_{ti}/v_A and for parameters of relevance to the simulation. The damping becomes significant as the argument of the Z function appearing in Eq. (6) approaches one. The solid curve in Fig. 12 corresponds to the ion temperature used in the PIC results shown later in Figs. 13 and 14. It is seen from Fig. 12 that the damping is strongest for low wave numbers, which is somewhat counter intuitive but can be understood readily by making a small k_x expansion of the dispersion relation. The consequence of this damping is that it filters the low-k_x components and thus

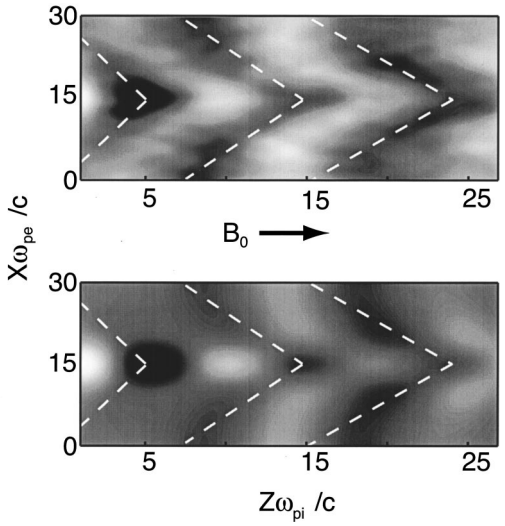

FIG. 13. Spatial pattern of y component of wave magnetic-field B_y at a fixed time shows inverted-cone behavior associated with hot ions for $\rho_i\omega_{pe}/c=1.1$ and $\omega=0.5\Omega_{ci}$. Light-shaded contour is positive y direction (out of page) and dark is negative. Top panel is the PIC result and bottom panel is the theoretical prediction. The dashed white lines are an aid to compare the key features; they are placed identically in both panels and demonstrate good agreement between theory and simulation. Figure 14 shows line cuts from these wave patterns.

enhances the cone features of the pattern radiated by the antenna.

Figure 13 shows the two-dimensional spatial pattern of the y component of the wave magnetic-field $B_y(x,z)$, for a shear Alfvén wave excited by the antenna at the left boundary, shown in Fig. 1, for a plasma with hot ions and cold electrons. The snapshot corresponds to a fixed time $\omega t=24$. The ion Larmor radius is $\rho_i=1.1c/\omega_{pe}$ and $\omega=0.5\Omega_{ci}$. The top panel corresponds to the simulation results. The simulation pattern has been clipped on the left and right sides to line up the peak intensity at the antenna with the presentation shown in the bottom panel. The pattern shown in the lower panel is the steady-state prediction for the shear Alfvén wave generated by propagating B_y using a generalization of Eq. (3) where the axial wave number $k_z(k_x)$ is obtained from a numerical solution for the kinetic dispersion relation with hot ions [Eqs. (5) and (6)]. It is seen that the wave patterns form conelike structures pointing away from the source in contrast with the orientation of the cones obtained for cold ions, as shown in Fig. 6. A comparison of the upper and lower panels shows agreement in the shape and wavelength of the wave patterns between the PIC simulation and the prediction of kinetic theory. However, the simulation wave pattern is distorted by the background noise whose magnitude is determined by the number of computer particles used. It can be extracted from the top panel that the simulation result has a $k_x=0$ compressional Alfvén wave mixed in, as is discussed in Sec. IV. This feature is not included in the theoretical wave pattern. The parasitic compressional Alfvén wave dominates the $k_x=0$ features since the shear Alfvén wave is strongly damped for small perpendicular wave numbers, as shown in Fig. 12. The mixing with the compressional mode causes some distortion of the shear-wave cones.

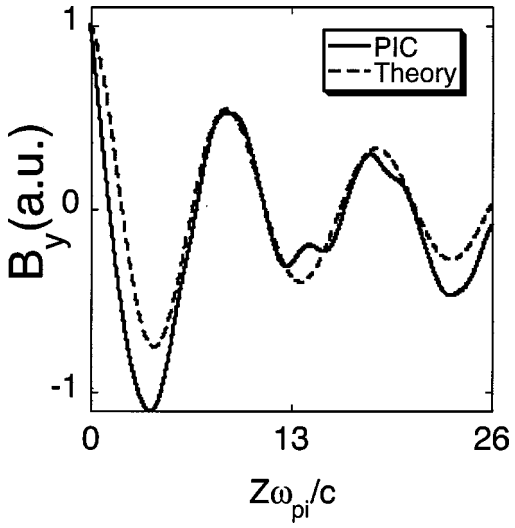

FIG. 14. Axial dependence of wave magnetic-field B_y at a fixed time shows damping of the wave by cyclotron resonance associated with finite frequency $\omega=0.5\Omega_{ci}$ and hot ions $\rho_1\omega_{pe}/c=1.1$. Solid curve is the simulation result and corresponds to a line cut in the top panel of Fig. 13 at fixed $x\omega_{pe}/c=14.0$. The dashed curve is the equivalent theoretical prediction extracted from the bottom panel of Fig. 13.

Figure 14 presents a quantitative comparison of the PIC result (solid curve) and the theoretical prediction (dashed curve). These results correspond to a cut at a fixed transverse position $x=14.0c/\omega_{pc}$ in the top and bottom panels of Fig. 13. The comparison of these two line cuts show good agreement in both the damping and wavelength between the simulation and theory.

VI. CONCLUSIONS

A particle-in-cell code has been developed that is capable of describing the propagation of Alfvén waves excited from a boundary. It has been demonstrated that the code correctly describes the properties of shear and compressional modes over a wide range of frequencies ($0.1\Omega_{ci}\leqslant\omega\leqslant 2.5\Omega_{ci}$) while retaining the full electron and ion dynamics. These features allow the study of Alfvénic interactions beyond the MHD description.

The code has been used to elucidate the properties of Alfvén wave cones radiated from sources having transverse scale comparable to the electron skin depth. As has been predicted theoretically[20] and previously confirmed in laboratory experiments,[18] the PIC results show that in the inertial regime the cones result in the spread of shear modes at a small angle relative to the confinement field. The theoretical prediction for the value of the inertial cone angle has been tested for the higher frequency regime ($\omega=0.5\Omega_{ci}$) where deviations arise between the $\mathbf{E}\times\mathbf{B}$ currents carried by ions and electrons. Good agreement between the theoretical prediction and the simulation results is found in this regime as well as at lower frequencies where cancellation between these currents occurs.

An investigation has been undertaken of the effect of hot ions on the Alfvén wave cones. As is expected from the kinetic dispersion relation, the PIC simulations demonstrate that as the ion temperature is increased there is a reversal in

the cone angle. The reversal implies that there is a cross-field focusing of the shear Alfvén waves. This is an effect which is presently being considered in studies of field line resonances in the earth's magnetic field. The PIC results also illustrate the damping of shear modes due to the Doppler-shifted cyclotron resonance with hot ions. This is a process of relevance to signals whose frequency is a significant fraction of the ion gyrofrequency in high-β plasmas.

It is anticipated that with the enhancements in computing power expected in the near future, the code demonstrated in this study will provide useful insight into the exploration of nonlinear Alfvénic interactions of relevance to laboratory and space investigations.

ACKNOWLEDGMENTS

This work was sponsored by NSF Grant No. ATM-0138187. The original OSIRIS code was developed by Professor W. Mori's research group at UCLA to study laser-plasma interactions. The large simulations were performed in the Blue Horizon and Datastar computers operated by NPACI.

[1]For recent update consult *Radio Frequency Power in Plasmas: 14th Topical Conference*, edited by T. K. Mau and J. deGrassie, AIP Conf. Proc. No. 595 (AIP, New York, 2002).
[2]N. N. Gorelenkov, H. L. Berk, R. Budny, C. Z. Cheng, G. Y. Fu, W. W. Heidbrink, G. J. Kramer, D. Meade, and R. Nazikian, Nucl. Fusion **43**, 594 (2003).
[3]K. Stasiewicz, P. Bellan, C. Chaston, C. Kletzing, R. Lysak, J. Maggs, O. Pokhotelov, C. Seyler, P. Shukla, L. Stenflo, A. Streltsov, and J.-E. A. Wahlund, Space Sci. Rev. **92**, 423 (2000).
[4]C. A. Kletzing and S. Hu, Geophys. Res. Lett. **28**, 693 (2001).
[5]V. Genot, P. Louarn, and F. Mottez, J. Geophys. Res. **105**, 27611 (2000).
[6]C. C. Chaston, J. W. Bonnell, C. W. Carlsson, J. P. McFadden, R. E. Ergun, R. Strangeway, and E. J. Lund, J. Geophys. Res. **109**, A04205 (2004).
[7]B. T. Tsurutani, B. Buti, J. K. Arballo, T. Hada, E. J. Smith, and A. Balogh, Adv. Space Res. **28**, 765 (2001).
[8]P. K. Shukla, R. Bingham, J. F. McKenzie, and W. I. Axford, Solar Physics **186**, 61 (1999).
[9]A. Teufel, I. Lerche, and R. Schlickeiser, Astron. Astrophys. **397**, 777 (2003).
[10]B. R. Ragot, Astrophys. J. **536**, 455 (2000).
[11]J. E. Maggs and G. J. Morales, Phys. Rev. Lett. **91**, 035004 (2003).
[12]For a recent comprehensive survey consult N. F. Cramer, *The Physics of Alfvén Waves* (Wiley-VCH, Berlin, 2001).
[13]M. Temerin, J. McFadden, M. Boehm, and C. W. Carlson, J. Geophys. Res. **91**, 5769 (1986).
[14]R. Vainio and R. Schlickeiser, Astron. Astrophys. **343**, 303 (1999).
[15]C. K. Birdsall and A. B. Langdon, *Plasma Physics via Computer Simulation* (McGraw-Hill, New York, 1985).
[16]J. R. Wygant, A. Keiling, C. A. Cattell, R. L. Lysak, M. Temerin, F. S. Mozer, C. A. Kletzing, J. D. Scudder, V. Streltsov, W. Lotko, and C. T. Russel, J. Geophys. Res. **107**, SMP24-1-15 (2002).
[17]K. Ronnmark and M. Hamrin, J. Geophys. Res. **105**, 25333 (2000).
[18]W. Gekelman, D. Leneman, J. Maggs, and S. Vincena, Phys. Plasmas **1**, 3775 (1994).
[19]D. Leneman, W. Gekelman, and J. Maggs, Phys. Rev. Lett. **82**, 2673 (1999).
[20]G. J. Morales, R. S. Loritsch, and J. E. Maggs, Phys. Plasmas **1**, 3765 (1994).
[21]G. J. Morales and J. E. Maggs, Phys. Plasmas **4**, 4118 (1997).
[22]R. G. Hemker, Ph.D. thesis, UCLA, 2000.
[23]V. K. Decyk, C. D. Norton, and B. K. Szymanski, Sci. Prog. **6**, 363 (1997).
[24]E. L. Lindman, J. Comput. Phys. **18**, 66 (1975).
[25]N. A. Krall and A. W. Trivelpiece, *Principles of Plasma Physics* (McGraw-Hill, New York, 1973), p. 178.
[26]R. Rankin, J. Y. Lu, R. Marchand, and E. F. Donovan, Phys. Plasmas **11**, 1268 (2004).
[27]S. Ichimaru, *Basic Principles of Plasma Physics—A Statistical Approach* (Benjamin, New York, 1973), p.89.